AIAA JOURNAL
Vol. 47, No. 5, May 2009

Matrix-Free Methods for the Stability and Control of Boundary Layers

Shervin Bagheri,* Espen Åkervik,* Luca Brandt,† and Dan S. Henningson‡
Royal Institute of Technology, 100 44 Stockholm, Sweden

DOI: 10.2514/1.41365

This Lecture presents matrix-free methods for the stability analysis and control design of high-dimensional systems arising from the discretized linearized Navier–Stokes equations. The methods are applied to the two-dimensional spatially developing Blasius boundary layer. A critical step in the process of systematically investigating stability properties and designing feedback controllers is solving very large eigenvalue problems by storing only velocity fields at different times instead of large matrices. For stability analysis, in which the entire dynamics of perturbations in space and time is of interest, iterative and adjoint-based optimization techniques are employed to compute the global eigenmodes and the optimal initial conditions. The latter are the initial conditions yielding the largest-possible energy growth over a finite time interval. The leading global eigenmodes take the shape of Tollmien–Schlichting wave packets located far downstream in the streamwise direction, whereas the leading optimal disturbances are tilted structures located far upstream in the boundary layer. For control design, on the other hand, the input–output behavior of the system is of interest and the snapshot method is employed to compute balanced modes that correctly capture this behavior. The inputs represent external disturbances and wall actuation and the outputs represent sensors that extract wall shear stress. A low-dimensional model that captures the input–output behavior is constructed by projection onto balanced modes. The reduced-order model is then used to design a feedback control strategy such that the growth of disturbances is damped as they propagate downstream.

I. Introduction

CONTROL of wall-bounded transitional and turbulent flows has been the subject of several research efforts, owing to the high potential benefits. In these fluid-mechanics systems, due to the large flow sensitivity, dramatic effects on global flow parameters may be achieved by minute local perturbations using devices sensing and acting on only small parts of the flow with a small amount of energy. Such control devices can be used to obtain reduction of the skin-friction drag, for example, implying relevant savings of the operational cost of commercial aircraft and cargo ships.

In this Lecture, we perform stability analysis and control design for the Blasius flow. The work is motivated by the need to provide efficient numerical tools to analyze complex flows and to design efficient control strategies. Although we present results for the Blasius flow, the methodology is applicable to any complex flow described by the linearized Navier–Stokes equations. The techniques in this Lecture share a common methodology: very large eigenvalue problems are solved based only on snapshots of the velocity field at different points in time. No large matrices are stored. Therefore, the main tool is a code that integrates the forward and adjoint linearized Navier–Stokes equations in time. This so-called time-stepper technique has become increasingly popular in both stability analysis [1–3] and in control design [4].

It is now well understood that wall-bounded flows are very sensitive to specific perturbations [5]. In particular, boundary-layer flows support convective instabilities and behave as noise amplifiers [6]. Convectively unstable shear flows are stable from a global point of view [6,7]; wave packets generated locally grow in amplitude as they travel downstream and finally decay or leave the observation window. This behavior can be captured by a nonmodal analysis (see, for example, [8]). It is therefore meaningful to analyze the spatial structure of the initial conditions and forcing, yielding the largest-possible energy growth over a finite time interval. This optimization problem can be solved efficiently for complex flows by solving the direct and adjoint Navier–Stokes equation for the linear evolution of perturbation about a steady state, as shown here (see also [1] or [9]).

Dan S. Henningson is a Professor of fluid mechanics in the Department of Mechanics at the Royal Institute of Technology (KTH), Stockholm, Sweden. He obtained his undergraduate degree from the same institute and his M.S. in aeronautics and astronautics from Massachusetts Institute of Technology (MIT) in 1985. His Ph.D. was obtained at KTH in 1988, after which he started as an Assistant Professor in the Department of Mathematics at MIT. In 1992 he came back to Sweden to work as a Senior Scientist at the Aeronautical Research Institute of Sweden (FFA). At the same time, he was an Adjunct Professor at the Department of Mechanics at KTH. In 1999 he became a full Professor in the same department, and since 2005 he has served as its head. Professor Henningson has also been involved in a number of Centers of Excellence. He had been the Founding Director of the KTH Center for Computational Science and Engineering (KCSE), organizing all of the computational activities at KTH, and now serves as the Chairman of its Board. Since 2006, he has been the Founding Director of the Linné Flow Centre, organizing all fundamental fluid mechanics research at KTH. Professor Henningson is the author of numerous articles and conference proceedings in the area of stability, transition, and flow control and now serves as an Associate Editor of the *Journal of Fluid Mechanics*. He is also the author of the book *Stability and Transition in Shear Flows*.

Presented as Paper 4099 at the 5th AIAA Theoretical Fluid Mechanics Conference, Seattle, WA, 23–26 June 2008; received 2 October 2008; revision received 26 January 2009; accepted for publication 26 January 2009.

*Graduate Student, Department of Mechanics.
†Assistant Professor, Department of Mechanics.
‡Professor, Department of Mechanics.

Two aspects in flow control have been identified as crucial to apply feedback control in more complex flows and to move toward an implementation in wind-tunnel tests:

1) Model reduction significantly decreases the cost of both constructing the controller and running it online, thus allowing the fast computation of the control signal directly from the sensor output.

2) There is a need to naturally consider localized sensors and actuators.

Both of these aspects are addressed by Bagheri et al. [4]. In this Lecture, the results of [4] are extended by introducing wall actuation and wall shear stress measurements instead of idealized volume forcing actuation and velocity measurements inside the flow. The incorporation of actuators and sensors at the physical boundaries in our design takes us one step closer to use the controller in actual experiments.

Recently, several groups have suggested and pursued the combination of computational fluid dynamics and control theory, thus going past early attempts of flow control based on physical intuition or on a trial-and-error basis (see the review in [10]). The reader is also referred to Bagheri et al. [11] for a thorough review of the many tools used in flow control. In early work from our group [12–14], a linear model-based feedback control approach that minimizes an objective function that measures the perturbation energy is formulated in which the Orr–Sommerfeld and Squire equations model the flow dynamics. The latter equations describe the linear evolution of perturbations evolving in a parallel base flow. The control problem is combined with a state estimator. The so-called Kalman and extended Kalman filters have been implemented to reconstruct the flow in an optimal manner by only considering continuous wall measurements. These studies have also shown the importance of physically relevant stochastic models for the estimation problem [15,16], in which stochastic noise needs to accurately describe the unmodeled dynamics such as uncertainties and nonlinearities. Based on these models, the estimator is shown to work for both infinitesimal and finite amplitude perturbations in direct numerical simulations of transitional flows [17,18]. However, these studies assumed a parallel base flow and distributed sensing and actuation at the wall.

Model reduction becomes essential to apply modern control theoretical tools to fluid flow systems. For linear control, the aim is to build a model of low dimension that captures the input–output behavior of the Navier–Stokes system and to use this model for optimal feedback control design. Balanced truncation [19] is a method for model reduction that takes into account both the flow structures most easily influenced by the input and the flow structures to which the outputs are most sensitive. The method provides a set of biorthogonal modes, called the balanced modes, that serve as a projection basis for model reduction. The method employed to compute the balanced modes is the snapshot-based balanced truncation introduced by Rowley [20]. This method has been recently applied to the channel flow [21], the flow around a pitching airfoil [22], and the Blasius flow [4].

The Lecture is organized as follows: The modal and nonmodal stability analysis is presented in Sec. II. We start with describing the flow setup and formulating two eigenvalue problems. We continue with showing how the eigenvalue problems can be solved iteratively and, finally, present results for the Blasius flow. Section III deals with the control design. We introduce inputs and outputs and write the system in the state-space formulation. A brief summary of the linear quadratic Gaussian (LQG) framework is provided before model reduction based on balanced modes is introduced. The snapshot method used for model reduction is explained, and results on the performance of the reduced-order and controller are shown. Section IV provides concluding remarks.

II. Stability Analysis

A. Flow Configuration and the Initial Value Problem

We consider the two-dimensional incompressible flow over a flat plate with constant freestream velocity U_∞, as shown in Fig. 1. Starting from the leading edge, a viscous boundary layer evolves downstream. The evolution of the streamwise velocity u, the wall-normal velocity v, and the pressure p in time t and space (x_1, x_2) is governed by the incompressible nonlinear Navier–Stokes equation [23]. Our analysis deals with the evolution of infinitesimal perturbations on this laminar boundary-layer solution and is limited to the computational domain shown by the gray area in Fig. 1. The inflow boundary is set to the downstream position corresponding to a Reynolds number $Re_{\delta_0^*} = U_\infty \delta_0^* / \nu = 1000$, where δ_0^* is the local displacement thickness of the boundary layer and ν is the kinematic viscosity. Throughout the Lecture, all variables are nondimensionalized by U_∞ and δ_0^*. The length and height of the domain are $L_x = 1000$ and $L_y = 30$ in the streamwise direction x_1 and wall-normal direction x_2, respectively.

The steady state, about which a linearization is performed, is obtained by marching the nonlinear governing equations in time. The discretized and linearized Navier–Stokes equations with boundary conditions can be cast as an initial value problem:

$$\dot{\mathbf{u}}(t) = \boldsymbol{A}\mathbf{u}(t) \qquad \mathbf{u}(0) = \mathbf{u}0$$

where $\mathbf{u} = (u, v)^T$. However, for two- or three-dimensional base flows the system matrix $\boldsymbol{A}$ will have very large dimension (i.e., the number of grid points times the number of velocity components $n = 2N_xN_y$). Our analysis will therefore be based on the solution of the linearized Navier–Stokes equations that can be represented by the matrix exponential (also referred to as the evolution operator):

$$\mathbf{u}\,(t) = \boldsymbol{T}(t)\mathbf{u}(0) = e^{\boldsymbol{A}t}\mathbf{u}_0$$

The matrix exponential $\boldsymbol{T}(t)$ is the key to both stability analysis and control design, which will be discussed in the subsequent sections. However, this discrete operator also poses the greatest computational challenge, due to its dimension. For example, the storage of the one-dimensional Orr–Sommerfeld matrix for the evolution of disturbances in parallel flows requires approximately 1 MB of memory, the system matrix for the present spatially inhomogeneous flow with the numerical scheme introduced previously requires approximately 200 GB, and the memory usage for a full three-dimensional system would be of the order of 200 TB.

However, the action of $\boldsymbol{T}(t)$ on any flowfield simply amounts to integrating the Navier–Stokes equations in time. In what follows, the reader should equate $\boldsymbol{T}(t)\mathbf{u}(s)$ with a direct numerical simulation (DNS) starting with an initial condition $\mathbf{u}(s)$ and providing $\mathbf{u}(t+s)$ at a later time. In this so-called time-stepper approach, system matrices are never stored and storage demands in memory are of the same order as a small number of flowfields. Numerically, the equations are solved with the pseudospectral DNS code described in [24], in which the spatial operators are approximated by Fourier expansion in the streamwise direction with $N_x = 768$ equally distributed points and Chebyshev expansion in the wall-normal direction on $N_y = 101$ Gauss–Lobatto collocation points. A fringe region enforces periodicity in the streamwise direction [25].

B. Modal Stability

The first step in the understanding of the fluid problem at hand is examining the hydrodynamic stability of the flow (i.e., the behavior of infinitesimal disturbances to a base flow). In particular, modal stability deals with the response behavior of the base flow to disturbances as time tends to infinity and is determined by the eigenvalues of $\boldsymbol{A}$:

$$\boldsymbol{A} = \boldsymbol{U}\boldsymbol{\Lambda}\boldsymbol{U}^{-1} \tag{1}$$

where the columns of the matrix $\boldsymbol{U}$ contain the global modes, the columns of $\boldsymbol{U}^{-1}$ contain the adjoint global modes (i.e., $\boldsymbol{U}^{-1}\boldsymbol{U} = \boldsymbol{I}$), and the diagonal matrix $\boldsymbol{\Lambda}$ contains the eigenvalues λ_j of $\boldsymbol{A}$. As mentioned previously, in many cases, only instantaneous velocity fields at different times are available, not matrices. To use the time-stepper technique explained in Sec. II.D, it is convenient to rewrite the eigenvalue problem (1) in terms of the evolution operator:

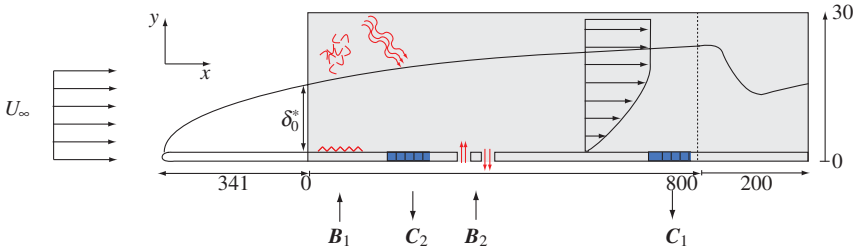

Fig. 1 Configuration used for the control of perturbations in a two-dimensional flat-plate geometry. The computational domain $\Omega = (0, L_x) \times (0, L_y)$, shown by the gray region, extends from $x = 0$ to 1000 with the fringe region starting at $x = 800$. The first input B_1, located at $(x_w, y_w) = (35, 1)$, models the initial receptivity phase, in which disturbances are induced by freestream turbulence, acoustic waves or wall roughness. The actuator B_2 provides a mechanism to manipulate the flow: in this case, by a wall blowing and suction centered at $x_u = 400$. Two sensors C_1 and C_2, measuring the skin friction near the wall, are located at $x_y = 300$ and $x_z = 750$, respectively. The upstream measurements are used to estimate the incoming perturbations, and the downstream sensor quantifies the effect of the control.

$$\boldsymbol{T}(t) = \boldsymbol{U}\boldsymbol{\Sigma}\boldsymbol{U}^{-1} \tag{2}$$

where $\boldsymbol{\Sigma} = \exp(\boldsymbol{\Lambda} t)$. Note that the evolution operator for a fixed t has the same eigenfunctions as $\boldsymbol{A}$. The temporal growth rate and the frequency of the eigenmodes are given by

$$\mathrm{Re}(\lambda_j) = \ell_n(|\sigma_j|)/t \qquad \mathrm{Im}(\lambda_j) = \arg(\sigma_j)/t$$

respectively, with $\boldsymbol{\Sigma} = \mathrm{diag}(\sigma_1, \ldots, \sigma_n)$. If $\mathrm{Re}(\lambda_j) > 0$ (or $|\sigma_1| > 1$), the flow is linearly globally unstable.

C. Nonmodal Stability

The amount of information obtained from Eq. (2) is limited to the asymptotic flow response and does not reveal the short-time behavior of disturbances inherent to many flow systems. Relevant transient growth [5] of perturbations is indeed observed for many fluid dynamic systems due to the nonnormality of the operator $\boldsymbol{A}$ (an operator that does not commute with its adjoint), and nonmodal analysis is concerned with finding instabilities that are amplified in a finite time interval. Furthermore, a competition between nonmodal and modal growth is observed in many systems: for example, for three-dimensional perturbations in the Blasius boundary layer [26]. For such flows, different transition scenarios can be observed, depending on the external ambient noise. Therefore, to examine the largest-possible disturbance growth due to all possible unit-norm initial conditions $\mathbf{u}_0$, we will consider the energy associated with the disturbance at any time t:

$$\|\mathbf{u}(t)\|^2 = (\boldsymbol{T}(t)\mathbf{u}_0, \boldsymbol{T}(t)\mathbf{u}_0) = (\mathbf{u}_0, \boldsymbol{T}^*(t)\boldsymbol{T}(t)\mathbf{u}_0) \tag{3}$$

In the preceding expression, the perturbation kinetic energy is the relevant norm and the adjoint evolution operator $\boldsymbol{T}^*(t)$ is introduced. Applying this operator corresponds to the integration of an adjoint state from time t to time 0. One can show [4] that an initial value problem for the adjoint linearized Navier–Stokes equations governed by $\boldsymbol{A}^*$ but with negative time derivative can be associated with the adjoint evolution operator $\boldsymbol{T}^*$. For a derivation of the adjoint operators in general, we refer to [27], and for this particular setup, we refer to [4].

Initial conditions experiencing the largest nonmodal growth at time t correspond to the leading eigenvalues of the operator $\boldsymbol{T}^*(t)\boldsymbol{T}(t)$: that is,

$$\boldsymbol{T}^*(t)\boldsymbol{T}(t) = \boldsymbol{U}\boldsymbol{\Sigma}\boldsymbol{U}^* \tag{4}$$

In this Lecture, the eigenmodes of all matrices are denoted by $\boldsymbol{U}$, and it is clear from the context with which matrix they are associated. The first unit-norm eigenvector $\mathbf{u}_1$ is the optimal initial condition, resulting in the largest energy growth at time t. If its corresponding eigenvalue is larger than 1, $\sigma_1 > 1$, the system can support nonmodal growth. The corresponding flow state at time t can be found by the evaluation of $\boldsymbol{T}(t)\mathbf{u}_1$. To obtain a full map of the potential for transient growth, the computations are repeated for different times t.

D. Iterative Time-Stepping Technique

The eigenvalue problems defined in Eqs. (2) and (4) provide information about the modal and nonmodal flow behavior of the system, respectively. The dimensions of the matrices in Eqs. (2) and (4) are too large to be solved by direct methods, such as the standard QR method [28] (the decomposition of a matrix into an orthogonal and a triangular matrix). Therefore, one has to resort to iterative methods, such as the Arnoldi [29], which is based on the projection of the large matrix onto a lower-dimensional subspace $m \ll n$. This results in a significantly smaller system that can be solved with direct methods. In addition, as mentioned previously, in many cases, only instantaneous velocity fields at different times are available. A particular subspace is the Krylov $\mathcal{K}$ spanned by snapshots taken from flowfields separated by a constant time interval Δt:

$$\mathcal{K} = \mathrm{span}\{\mathbf{u}_0, \boldsymbol{F}(\Delta t)\mathbf{u}_0, \boldsymbol{F}(2\Delta t)\mathbf{u}_0, \ldots, \boldsymbol{F}((m-1)\Delta t)\mathbf{u}_0\}$$

where $\boldsymbol{F}(t) = \boldsymbol{T}(t)$ (modal stability) or $\boldsymbol{F}(t) = \boldsymbol{T}^*(t)\boldsymbol{T}(t)$ (nonmodal stability), and $\mathbf{u}_0$ is the initial guess that should contain nonzero components of the eigenmodes (it is usually chosen as random noise).

For modal stability analysis, every basis vector of the Krylov subspace is created by a numerical simulation of Δt. The actual time step of these simulations depends on the Courant–Friedrichs–Lewy condition and is much smaller than the sampling period Δt. The global spectrum using both the matrix method (i.e., storing matrix $\boldsymbol{A}$) and the time-stepper method is discussed further in the next section. See [3] for the application of this technique on a fully three-dimensional flow, where the size of the problem ($\boldsymbol{A}$ would be approximately a $10^7 \times 10^7$ matrix) prohibits matrix methods. Note that the eigenmodes of $\boldsymbol{T}$ are the same as those of the system matrix $\boldsymbol{A}$ only if Δt is chosen properly (i.e., so that it reflects the characteristic time scale of the physical structures in the flow). More specifically, the choice Δt is a balance between the time scale given by the Nyquist criterion and a sufficient temporal separation of the Krylov vectors to ensure convergence of the iterative method. Frequencies larger than the Nyquist frequency (i.e., $\omega > \omega_c = \pi/\Delta t$) are spuriously moved into the range of $\omega < \omega_c$. To avoid aliasing, Δt must therefore be small enough to include two sampling points in one period of the highest-frequency mode. In Fig. 2, the aliasing phenomenon is illustrated. The time stepper with $\Delta t = 30$ (squares) has Nyquist frequency $\omega_c = 0.1$ and therefore captures all frequencies in the range [0, 0.1] correctly. The time stepper with $\Delta t = 40$ (circles) has $\omega_c = 0.07$, and all frequencies higher than 0.07 are therefore mapped into [0, 0.07].

For nonmodal stability, every basis vector of the Krylov subspace is first constructed by a numerical simulation of Δt yielding the flowfield at $t = \Delta t$, which is then used as an initial condition for numerical simulation of the adjoint system backward in time for Δt.

The Krylov subspace $\mathcal{K}$ is orthonormalized with an m step Arnoldi factorization yielding the unitary basis $\boldsymbol{V}$ on the which $\boldsymbol{F}$ can be projected on

$$\boldsymbol{F}(\Delta t) \approx \boldsymbol{V}\boldsymbol{R}\boldsymbol{V}^*$$

This leads to a small $m \times m$ eigenvalue problem of the upper

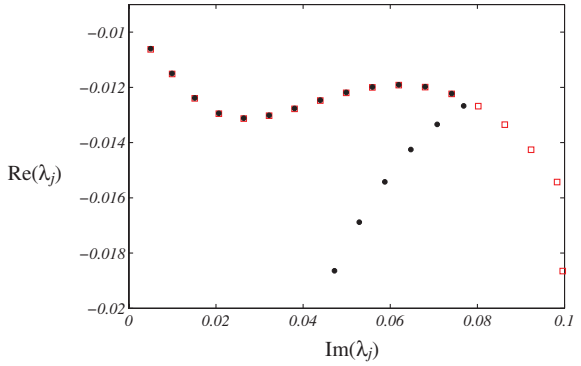

Fig. 2 Spectrum of the 2-D Blasius flow computed using the time-stepping technique with $\Delta t = 30$ (squares) and $\Delta t = 40$ (circles). The high-frequency eigenvalues of the latter computation are mapped/aliased into the low-frequency domain.

Hessenberg matrix $\boldsymbol{R}$,

$$\boldsymbol{RS} = \boldsymbol{\Sigma S}$$

which can be computed by standard methods such as the QR algorithm. A number of the so-called Ritz values $\boldsymbol{\Sigma} = \mathrm{diag}(\sigma_1, \ldots, \sigma_m)$ typically converge rapidly to the eigenvalues of the large system $\boldsymbol{F}$. The eigenmodes corresponding to the m converged eigenvalues with the largest magnitude are recovered by $\boldsymbol{U} = \boldsymbol{VS}$.

Note that one does not know beforehand how large the Krylov subspace (i.e., m) has to be to converge to the desired number of eigenvalues. An implicitly restarted Arnoldi algorithm (IRAM) [30] implemented in the software package ARPACK [29] can be used to restart the Arnoldi procedure with a new improved initial guess, $\mathbf{u}_0$, repeatedly until convergence. In this way, the Krylov subspace can be very small although the number of flowfield snapshots separated by Δt required for convergence can be very large. As an example, the number of snapshots required for convergence of the 22 eigenmodes in [3] was 1800, however, thanks to IRAM, the Krylov subspace was only of the order $m \approx 60$.

E. Results

Results on modal and nonmodal stability of the two-dimensional perturbations of the Blasius boundary layer are presented in this section. As mentioned previously, the flow under investigation here is locally unstable but globally stable. Locally unstable perturbations, the Tollmien–Schlichting waves, grow while traveling downstream, eventually leaving our control domain. From a global point of view, the flow is then stable, because disturbances have to be continuously fed upstream to avoid that the flow returns to its undisturbed state at each streamwise position. However, a significant transient growth of the disturbance energy in the domain is associated with the propagation of the wave packet [31,32]. This is also referred to as streamwise nonnormality [7,33].

1. *Modal Stability*

For two-dimensional perturbations of the Blasius boundary-layer flow, the memory requirements are still small enough to enable the storage of the system matrix $\boldsymbol{A}$ in memory; the leading eigenmodes from the matrix eigenvalue problem (1) can thus be obtained by means of the shift and invert Arnoldi procedure. Figure 3a shows the eigenvalues obtained by the shift and invert matrix method as black circles. In the spectrum, one can identify several branches that all can be related to corresponding modes in the spectrum of a parallel Blasius boundary layer, as found by solving the Orr–Sommerfeld equations, though modified by nonparallelism and boundary conditions [32]. The upper branch can be identified as pure Tollmien–Schlichting (TS) waves. These modes are characterized by slightly damped eigenvalues, with the corresponding eigenvectors obtaining their maximum values inside the boundary layer and decaying exponentially in the freestream. More stable modes can be associated with the continuous spectrum: that is, modes oscillating in the freestream and decaying inside the boundary layer.

Figures 3b and 3c show two examples of TS eigenvectors associated with eigenvalues marked as k_1 and k_2 in Fig. 3a. As a consequence of the convective nature of the instabilities arising in the Blasius flow, where disturbances grow in amplitude as they are convected in the downstream direction, the global eigenmodes are located far downstream, where the flow energy is the largest. The wall-normal structures of these modes are very similar to those obtained by local temporal analysis in the framework of the Orr–Sommerfeld equation. The amplitude of the waves is exponentially increasing downstream: this, together with the temporal decay rate given by the eigenvalue, accounts for the spatial behavior of the mode. The matrix-free method based on the time stepper introduced in Sec. II.D successfully locates the least damped eigenvalues by solving the eigenvalue problem (2). The eigenvalues are shown as squares in Fig. 3a and are in perfect agreement with the results obtained by the matrix method.

Note that all the eigenvalues are damped, indicating that we will never observe the evolution of single eigenmodes in the flow, but we should rather focus our attention on the nonmodal behavior: in other words, the transient-growth scenario. It is possible to project the system (3) on a set of eigenmodes obtained from Eq. (2), thereby approximating the flow dynamics by a low-dimensional model living in the space spanned by a finite number of eigendirections [5]. For globally unstable flows, only one or a few eigenmodes may be sufficient to capture the physical mechanism of the instability (see, for example, the shallow rounded cavity flow in [34], in which an oscillating cycle could be captured by the sum of two unstable

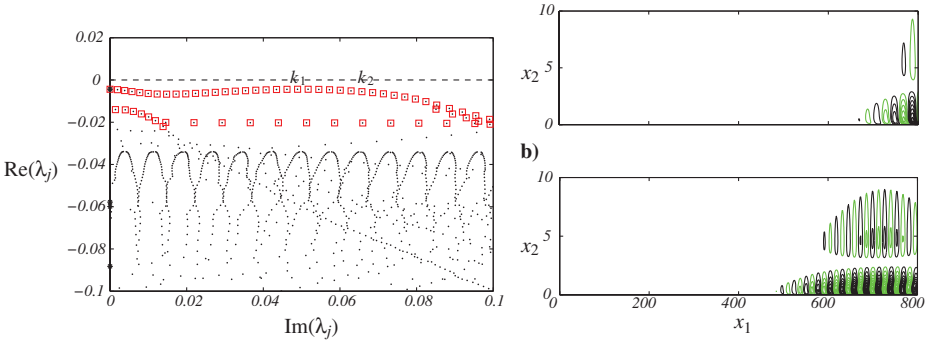

Fig. 3 Plots of a) eigenvalues of A as computed by the shift and invert Arnoldi method (shown as black circles) and eigenvalues computed by time stepping using the evolution operator $T(t)$ (shown as magenta squares) (the slightly damped eigenvalues, corresponding to Tollmien–Schlichting (TS) modes, and the freestream propagating modes are found by both methods), b) streamwise velocity component of the least stable TS eigenvectors, marked as k_1 in the first plot, and c) streamwise velocity component of a high frequency but more damped TS mode, marked as k_2 in the first plot.

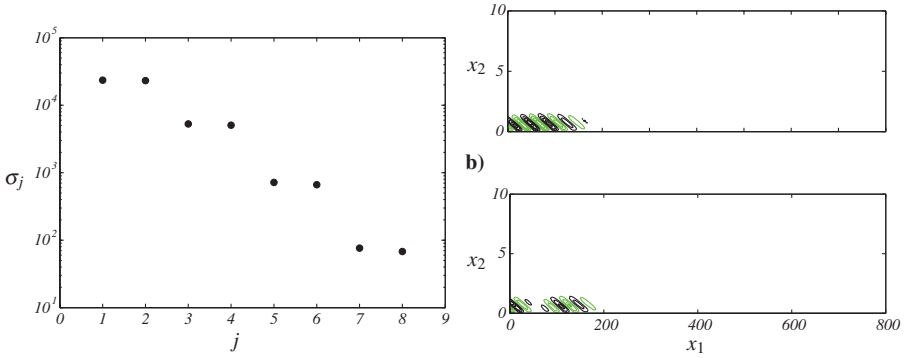

Fig. 4 Plots of a) eigenvalues of T^*T computed using the forward and adjoint time-stepper with $t = 1800$, b) streamwise velocity component of the optimal disturbance corresponding the largest eigenvalue in the first plot, and c) streamwise velocity component of a suboptimal, corresponding to the third largest eigenvalue in the first plot.

eigenmodes). However, for a boundary-layer flow such as that studied here, it is shown in [32] that $\mathcal{O}(1000)$ eigenmodes are needed to capture the full instability mechanism. With the present discretization and boundary conditions, moreover, the sum of the 1500 eigenmodes obtained from the Arnoldi method is not able to correctly describe the Orr mechanism [5,32,35,36] as obtained by the optimization via the time stepper defined in Eq. (4). This is most likely due to the presence of eigenmodes related to the fringe region among the least damped eigenmodes. This points to the limitations of using eigenvalues as a general tool to study stability of complex systems characterized by strong nonnormality.

2. *Nonmodal Stability*

Figure 4 shows the spectrum and two eigenfunctions of the eigenvalue problem (4) computed using the time stepper with $t = 1800$. Because $\boldsymbol{T}^*\boldsymbol{T}$ is a self-adjoint positive-definite operator, its eigenvalues are real and positive. Moreover, the eigenvalues shown in Fig. 4a come in pairs with similar magnitudes. The corresponding velocity fields have the same wave packet structure 90 deg out of phase, representing traveling structures. The most unstable modes (i.e., the optimal disturbance and a suboptimal mode) are shown in Figs. 4b and 4c. They both have a spatial support far upstream, where the sensitivity of the flow is the largest. The modes are tilted in the upstream direction, leaning against the shear layer. As noticed in [37], the upstream tilting of the optimal initial conditions can be attributed to the wall-normal nonnormality of the governing operator; perturbations extract energy from the mean shear by transporting momentum down the mean velocity gradient (the so-called Orr mechanism). Also note the separation of the spatial support of the optimal disturbance modes shown in Figs. 4b and 4c (far upstream) and the global eigenmodes shown in Figs. 3b and 3c (far downstream). This separation is associated with streamwise nonnormality of the system [7]. Finally, note that there is nearly 1 order of magnitude between the energy of first pair and second pair of eigenvalues shown in Fig. 4a. As a consequence, one can expect a selection of disturbances in a randomly forced flow that resembles the flow response obtained when using the optimal disturbance as the initial condition.

The energy evolution when solving for the largest eigenvalues of Eq. (4) at times $t = \{100, 200, \ldots, 2000\}$ is reported in Fig. 5a. When optimizing for short times, the optimal initial condition consists of upstream-tilted structures that exploit the Orr mechanism only [32] to extract energy from the flow. Increasing the optimization time, the upstream-tilted structures move upstream, toward the start of our computational domain, weighting the possibility of growth due to the local Orr mechanism with the energy gain associated with the amplification and propagation of TS waves. The maximum energy growth in this box is obtained for final time $t = 1800$. The corresponding optimal initial condition is shown in the top frame in Fig. 6. In Fig. 5b, we compare the energy evolution due to this optimal initial condition with the energy evolution obtained when projecting Eq. (4) onto the space spanned by a small number of modes: all modes included in the TS branch in Fig. 3. The evolution in the reduced system clearly does not capture the initial energy gain due to the Orr mechanism; however, by rescaling the energy curve and shifting it in time to account for the initial gain due to the Orr mechanism, the subsequent evolution (amplification and propagation of the TS waves) is almost perfectly matching that of the full system.

The detailed evolution of the streamwise velocity due to the optimal initial condition at time $t = 1800$ is shown in Fig. 6. At the initial time, the structures are leaning backward against the shear. During the initial phase of the development, the disturbance is raised

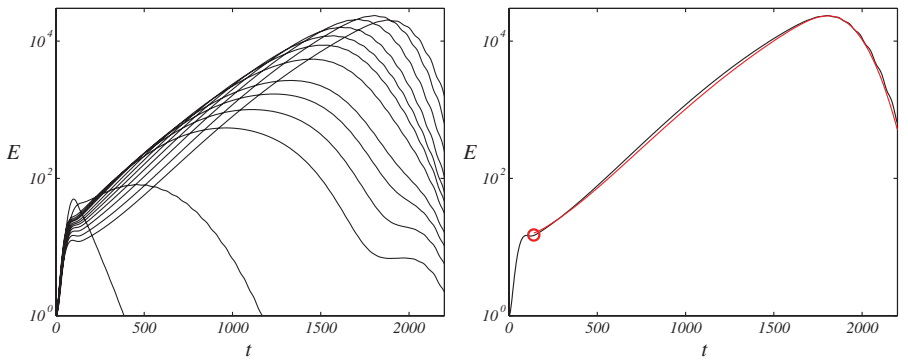

Fig. 5 Plots of a) energy growth when optimizing for different times (the maximum is achieved for time $t_m = 1800$ for which the maximum energy is $E = 2.35 \times 10^4$) and b) the energy evolution leading to the maximum growth at $t_m = 1800$ (thin black line) and the energy evolution obtained when projecting the system onto a small number of eigenvectors related to the TS branch in Fig. 3a (thick magenta line).

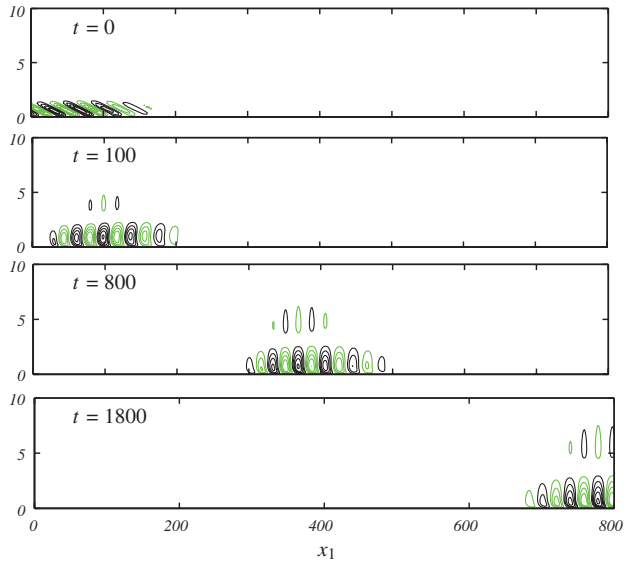

Fig. 6 Time evolution for streamwise velocity with the combined Orr and TS mechanism, when initiated with the optimal initial condition from $t = 1800$. Note that the maximum amplitude is growing from frame to frame following the energy evolution given in Fig. 5b.

up, gaining energy through the Orr mechanism [5,35,36] and forming a wave packet consisting of TS waves. The wave packet then propagates downstream, grows in size, and finally leaves the computational domain; the energy evolution for this flow is reported in Fig. 5b.

III. Control Design

A. Introducing Inputs and Outputs

The next step after the analysis of the internal dynamics of our linear system is to manipulate it or to control it. In particular, our objective is to minimize the perturbation energy resulting from the growth of instabilities during the transition process to suppress or delay turbulence. To this end, we introduce the inputs $\boldsymbol{B}_1$ and $\boldsymbol{B}_2$ and the outputs $\boldsymbol{C}_1$ and $\boldsymbol{C}_2$:

$$\dot{\mathbf{u}}(t) = \boldsymbol{A}\mathbf{u}(t) + \boldsymbol{B}_1 w(t) + \boldsymbol{B}_2 \phi(t) \tag{5}$$

$$z(t) = \boldsymbol{C}_1 \mathbf{u}(t) + l\phi(t) \tag{6}$$

$$y(t) = \boldsymbol{C}_2 \mathbf{u}(t) + \alpha g(t) \tag{7}$$

The linearized Navier–Stokes equations represented by $\boldsymbol{A}$ are now forced with external disturbances represented by the term $\boldsymbol{B}_1 w(t)$. These external disturbances may enter the boundary layer upstream through some receptivity mechanism such as freestream turbulence or acoustic waves interacting with roughness, as shown schematically in Fig. 1.

In practice, the entire spatiotemporal evolution of disturbances is not available, and it is therefore necessary to monitor the disturbance behavior through measurements. To accomplish this task, two sensors, $\boldsymbol{C}_1$ and $\boldsymbol{C}_2$, are introduced that measure the shear stress near the wall. The partial information of the incoming perturbations provided from the first sensor measurements ($\boldsymbol{C}_2$ in Fig. 1) is used to reconstruct the actual flow dynamics by using a Kalman filter. Based on this flow estimation, we can alter the behavior of disturbances by injecting fluid through blowing/suction holes in the wall. This type of actuation corresponds to imposing an inhomogeneous boundary condition $\mathbf{u}_w$ at the wall [see Eq. (B1) in Appendix B]. To pose the system in the standard state-space formulation commonly used in systems and control theory, the boundary term is lifted [38] into a volume forcing $\boldsymbol{B}_2\phi(t)$. In Appendix B, the lifting technique is demonstrated. The sensor output signal $y(t)$ is forced with noise $g(t)$ to model the uncertainty that may exist in the measurements under realistic conditions. The noise $g(t)$ can be considered as a third forcing, but rather than forcing the Navier–Stokes equations, it forces the measurements. Large values of the scalar α indicate a high level of noise corruption in the output signal, whereas for low values of α, the measurement $y(t)$ reflects information about the flowfield with high fidelity.

Measurements provided by the second sensor $\boldsymbol{C}_1$ located far downstream (see Fig. 1) is used to determine whether our controller has been successful in reducing the shear stress near the wall. It thus plays the role of an objective function[§]: that is,

$$\|z\|^2 = \int_0^\infty (\mathbf{u}^* \boldsymbol{C}_1^* \boldsymbol{C}_1 \mathbf{u} + l^2\phi^2)\mathrm{d}t \tag{8}$$

For large values of the scalar l, the control effort is considered to be expensive, whereas small values indicate inexpensive control.

The system with all inputs and outputs can be written in a compact state-space form:

$$\boldsymbol{G} := \begin{pmatrix} \boldsymbol{A} & \boldsymbol{B} \\ \boldsymbol{C} & \boldsymbol{D} \end{pmatrix} \tag{9}$$

where

$$\boldsymbol{B} = (\boldsymbol{B}_1, 0, \boldsymbol{B}_2) \in \mathcal{R}^{n\times 3}$$

contains the three input operators, and

$$\boldsymbol{C} = (\boldsymbol{C}_1, \boldsymbol{C}_2) \in \mathcal{R}^{2\times n}$$

contains the two output operators. The corresponding input time signals are

$$\boldsymbol{f}(t) = (w(t), g(t), \phi(t)) \in \mathcal{R}^{3\times 1}$$

and output time signals are

$$\boldsymbol{y}(t) = (y(t), z(t)) \in \mathcal{R}^{2\times 1}$$

In addition, the feedthrough term $\boldsymbol{D} \in \mathcal{R}^{2\times 3}$ is included to model the effects of measurement noise $g(t)$ and to penalize the actuation effort:

$$\boldsymbol{D} = \begin{pmatrix} 0 & 0 & l \\ 0 & \alpha & 0 \end{pmatrix}$$

Hereafter, the number of inputs and outputs will be denoted by p and r, respectively. The inputs and outputs used in the present study are given in Appendix A. The formal solution to input–output system (9) is

$$\boldsymbol{y}(t) = \boldsymbol{G}\boldsymbol{f}(t) = \boldsymbol{C}\int_0^t \boldsymbol{T}(t-\tau)\boldsymbol{B}\boldsymbol{f}(\tau)\mathrm{d}\tau + \boldsymbol{D}\boldsymbol{f}(t) \tag{10}$$

B. LQG/$\mathcal{H}_2$ Problem

The LQG/$\mathcal{H}_2$ framework provides a controller that minimizes the cost functional (8). It is appropriate if the system matrix $\boldsymbol{A}$ accurately describes the flow dynamics, although a precise knowledge of external disturbances and the degree of noise contamination of the measurements are not available. We refer to [11,40,41] for further details on the $\mathcal{H}_2$ control algorithm, as we will only outline the main steps here. The method can be extended (the so-called $\mathcal{H}_\infty$ method) to guarantee certain robustness properties. The control problem from an input–output viewpoint, or the $\mathcal{H}_2$ problem, can be formulated as follows:

Find an optimal control signal $\phi(t)$ based on the measurements $y(t)$ such that in the presence of external disturbances $w(t)$ and measurement noise $g(t)$, the output $z(t)$ is minimized.

[§]We assume that the cross weighting between the state and control signal is zero [39].

The determination of the control signal $\phi(t)$ is based only on the measurements $y(t)$ from the sensor $\boldsymbol{C}_2$. However, for linear systems, due to the separation principle [41], the feedback control law can be determined by assuming that the complete velocity field is known. The forcing needed to reproduce the flow only from wall measurements can be computed independently. Hence, the design of the $\mathcal{H}_2$ controller is performed by solving two quadratic matrix equations called Riccati equations [39] that are independent of each other. Solving the first Riccati equation, we obtain the feedback type of control signal $\phi(t) = \boldsymbol{K}\mathbf{u}(t)$. The second Riccati equation provides the estimation feedback gain $\boldsymbol{L}$ so that the observer

$$\dot{\hat{\mathbf{u}}}(t) = (\boldsymbol{A} + \boldsymbol{L}\boldsymbol{C}_2)\hat{\mathbf{u}}(t) + \boldsymbol{L}y(t)$$

can estimate the state $\hat{\mathbf{u}}$ from the wall stress measurements contained in $y(t)$. Finally, the controller is obtained by the combination of these two as (written in compact form)

$$\boldsymbol{G}_c := \begin{pmatrix} \boldsymbol{A} + \boldsymbol{B}_2\boldsymbol{K} + \boldsymbol{L}\boldsymbol{C}_2 & \boldsymbol{L} \\ \boldsymbol{K} & 0 \end{pmatrix} \tag{11}$$

This controller runs online next to the experiments. Based on wall shear stress measurements $y(t)$ extracted by the first sensor, it provides an optimal control signal $\phi(t)$ [i.e., $\phi(t) = \boldsymbol{G}_c y(t)$].

Any adequately accurate spatial discretization of the Navier–Stokes equations linearized about two- or three-dimensional base flows results in a system with at least $n \geq 10^5$ degrees of freedom. Because of the high-dimensional state space, we cannot, in general, solve the Riccati equations. Moreover, it would be very expensive to run the controller online, because it has the same dimension as the full system. For this reason, there is a desire to have a low-order controller (11) for the high-order Navier–Stokes system (also called the plant hereafter). The available methods can be broadly divided into two categories:

1) With controller reduction [42], a high-order controller $\boldsymbol{G}_c$ is first found and then a procedure is used to simplify it.

2) With model reduction, a low-order approximation of the plant $\boldsymbol{G}$ is first constructed and then a controller is designed.

In this Lecture, we will focus on the latter approach, because solving Riccati equations is not straightforward for $n \geq 10^5$.

C. Model Reduction Problem and Balanced Truncation

The main features of the flow behavior that are relevant to preserve in the reduced-order model are the input–output (I/O) behavior of the system (i.e., the relation between disturbances), wall actuation, and sensor outputs. Rather than investigating the entire dynamics of flowfields at different times, the I/O behavior considers the time signals $\boldsymbol{f}(t)$ and $\boldsymbol{y}(t)$. Fortunately, the I/O behavior has significantly simpler dynamics compared with stability analysis, in which the entire flow dynamics are under investigation.

The model reduction problem for the preservation of input–output dynamics can be posed as follows:

Find the state-space system of order $m \ll n$,

$$\boldsymbol{G}_m := \begin{pmatrix} \boldsymbol{Y}^*\boldsymbol{A}\boldsymbol{X} & \boldsymbol{Y}^*\boldsymbol{B} \\ \boldsymbol{C}\boldsymbol{X} & \boldsymbol{D} \end{pmatrix} = \begin{pmatrix} \boldsymbol{A}_m & \boldsymbol{B}_m \\ \boldsymbol{C}_m & \boldsymbol{D} \end{pmatrix} \tag{12}$$

so that for any input $\boldsymbol{f}(t)$, the difference between the output of the original $\boldsymbol{y}(t) = \boldsymbol{G}\boldsymbol{f}(t)$ and of the reduced system $\hat{\boldsymbol{y}}(t) = \boldsymbol{G}_m\boldsymbol{f}(t)$ is small: that is,

$$\sup_{\boldsymbol{f}} \frac{\|\boldsymbol{y} - \hat{\boldsymbol{y}}\|}{\|\boldsymbol{f}\|} = \|\boldsymbol{G} - \boldsymbol{G}_m\|_\infty \tag{13}$$

One way to compute the reduced-order model (12) with a nearly minimal model reduction error (13) is called balanced truncation [19]. To obtain the balanced reduced-order model (12) $\boldsymbol{G}_m$, we project Navier–Stokes equations including inputs and outputs ($\boldsymbol{G}$) onto the so-called balanced modes $\boldsymbol{X} \in \mathcal{R}^{n\times m}$. The modes are biorthogonal modes to adjoint balanced modes $\boldsymbol{Y} \in \mathcal{R}^{n\times m}$ (i.e., $\boldsymbol{Y}^*\boldsymbol{X} = I$).

The method to compute these modes can be introduced in many different ways. Traditionally, the balanced modes are defined as the eigenvectors of the product of the controllability and observability Gramian, defined as

$$\boldsymbol{P} = \int_0^\infty \boldsymbol{T}(\tau)\boldsymbol{B}\boldsymbol{B}^*\boldsymbol{T}^*(\tau)\mathrm{d}\tau \qquad \boldsymbol{Q} = \int_0^\infty \boldsymbol{T}^*(\tau)\boldsymbol{C}^*\boldsymbol{C}\boldsymbol{T}(\tau)\mathrm{d}\tau \tag{14}$$

The Gramians can be obtained by solving the Lyapunov equations:

$$\boldsymbol{A}\boldsymbol{P} + \boldsymbol{P}\boldsymbol{A}^* + \boldsymbol{B}\boldsymbol{B}^* = 0 \qquad \boldsymbol{A}^*\boldsymbol{Q} + \boldsymbol{Q}\boldsymbol{A} + \boldsymbol{C}^*\boldsymbol{C} = 0$$

In this section, we will outline the method in manner that is reminiscent of the optimization problems that arise in the stability analysis. The presentation closely follows Bagheri et al. [4], in which definitions of appropriate Hilbert spaces and adjoint operators are also provided. Whereas in stability analysis, we were concerned with the properties of the evolution operator $\boldsymbol{T}(t)$, our focus here will be on the so-called Hankel operator [43] that maps input signals to output signals. In particular, it is defined as the mapping from past inputs $\boldsymbol{f}(t)$: $t \in (-\infty, 0]$ to future outputs $\boldsymbol{y}(t)$: $t \in [0, \infty)$:

$$\boldsymbol{y}(t) = (\boldsymbol{H}\boldsymbol{f})(t) = \boldsymbol{C}\int_{-\infty}^{0} \boldsymbol{T}(t-\tau)\boldsymbol{B}\boldsymbol{f}(\tau)\mathrm{d}\tau$$

To determine $\boldsymbol{H}\boldsymbol{f}$, we decompose it into $\boldsymbol{H} = \boldsymbol{L}_o\boldsymbol{L}_c$ (shown schematically in Fig. 7).

First, we need to know the state at a reference time (say, $\mathbf{u}_0$) that results from driving the system with the input $\boldsymbol{f}(t)$:

$$\mathbf{u}_0 = \int_{-\infty}^{0} \boldsymbol{T}(-\tau)\boldsymbol{B}\boldsymbol{f}(\tau)\mathrm{d}\tau = \boldsymbol{L}_c\boldsymbol{f}(t)$$

The range of $\boldsymbol{L}_c$ [i.e., the restriction of the state-space to all possible initial states that we are able to reach with $\boldsymbol{f}(t)$] is called the controllable subspace. Second, we define the observability operator $\boldsymbol{L}_o$ as

$$\boldsymbol{y}(t) = \boldsymbol{C}\boldsymbol{T}(t)\mathbf{u}_0 = \boldsymbol{L}_o\mathbf{u}_0$$

which generates future outputs from the reference state. If $\boldsymbol{L}_o\mathbf{u}_0 = 0$ for an initial condition $\mathbf{u}_0$, then $\mathbf{u}_0$ is unobservable, because it cannot be detected by the sensors. Moreover, it is easy to verify that the Gramians are given by $\boldsymbol{P} = \boldsymbol{L}_c\boldsymbol{L}_c^*$ and $\boldsymbol{Q} = \boldsymbol{L}_o^*\boldsymbol{L}_o$ (see [4] for derivation of the adjoint operators $\boldsymbol{L}_c^*$ and $\boldsymbol{L}_o^*$).

Note that all inputs that give rise to the same $\mathbf{u}_0$ produce the same future output. Therefore, any two linearly independent reference states $\mathbf{u}_0$ result in linearly independent future outputs. Thus, the rank of the Hankel operator (i.e., the number of linearly independent outputs) is finite and equal to the minimal number of states required to realize the input–output behavior of the system. One might think that it is more natural to consider the input–output mapping $\boldsymbol{G}$ given by Eq. (10), but this operator is generally not of finite rank, which makes further analysis difficult [43].

The amplification of the output signal at time t is given by

$$\|\boldsymbol{y}(t)\|^2 = (\boldsymbol{H}\boldsymbol{f}(t), \boldsymbol{H}\boldsymbol{f}(t)) = (\boldsymbol{f}(t), \boldsymbol{H}^*\boldsymbol{H}\boldsymbol{f}(t))$$

In particular, the unit-norm input signals that result in the largest output response are the eigenmodes of $\boldsymbol{H}^*\boldsymbol{H}$ or the right singular

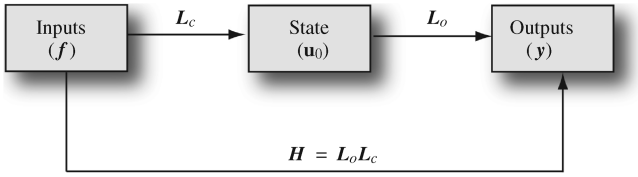

Fig. 7 The operators used to examine the system input–output behavior. The controllability operator L_c relates past inputs to the present state, and the observability mapping L_o relates the present state to the future outputs. Their combined action is expressed by the Hankel operator H.

vectors of $\boldsymbol{H}$: that is,

$$\boldsymbol{H} = \boldsymbol{U}\boldsymbol{\Sigma}\boldsymbol{V}^* \tag{15}$$

where the square root of the eigenvalues $\sigma_1 > \sigma_2 > \cdots$ are called the Hankel singular values (HSV). If $\sigma_1 > 1$, then the unit-norm input signal (the first column of $\boldsymbol{V}$) active in the past $t \in (-\infty, 0]$ will generate an amplified output signal in the future $t \in [0, \infty)$.

Using the mappings $\boldsymbol{L}_c$ and $\boldsymbol{L}_o$, we can now obtain the biorthogonal balanced modes:

$$\boldsymbol{X} = \boldsymbol{L}_c\boldsymbol{V}\boldsymbol{\Sigma}^{-1/2} \qquad \boldsymbol{Y} = \boldsymbol{L}_o^*\boldsymbol{U}\boldsymbol{\Sigma}^{-1/2} \tag{16}$$

Note that balanced modes contained in $\boldsymbol{X} = \{\mathbf{u}_1, \ldots, \mathbf{u}_m\}$ are flowfields obtained by mapping the most dangerous input signals $\boldsymbol{V}$ (i.e., right eigenvectors of $\boldsymbol{H}^*\boldsymbol{H}$) onto the state space using $\boldsymbol{L}_c$ (see [4] for further details).

The balanced reduced-order model is guaranteed to be asymptotically stable [44] if $\sigma_i \neq \sigma_{i+1}$. Moreover, upper and lower bounds [43] of the model reduction error for reduced-order model of order m are given by the HSV as

$$\sigma_{m+1} \leq \|\boldsymbol{G} - \boldsymbol{G}_m\|_\infty \leq 2\sum_{j=m+1}^{n} \sigma_j \tag{17}$$

D. Snapshot-Based Balanced Truncation

Standard balanced truncation is computed by solving two Lyapunov equations, which is not numerically feasible if $n > 10^5$, as the computational complexity is $\mathcal{O}(n^3)$ and storage requirement is $\mathcal{O}(n^2)$. Usually, the number of inputs and outputs are much smaller than the state dimension (i.e., $m, p \ll n$). Therefore, the input and output operators $\boldsymbol{L}_o$ and $\boldsymbol{L}_c$ have low numerical rank. In this section, a brief summary of the snapshot method [45] for solving the singular value decomposition (SVD) problem (15) is presented. The method for the computation of the balanced modes based on snapshots was introduced by [20], in which it is also described in more detail.

The integrals in Eq. (14) can be approximated by quadratures,

$$\boldsymbol{P} = \boldsymbol{L}_c\boldsymbol{L}_c^* \approx \sum_{j=1}^{k} \boldsymbol{T}(t_j)\boldsymbol{B}\boldsymbol{B}^*\boldsymbol{T}^*(t_j)\delta_j = \tilde{\boldsymbol{L}}_c\tilde{\boldsymbol{L}}_c^*$$

Similarly, for the observability Gramian, we have

$$\boldsymbol{Q} = \boldsymbol{L}_o^*\boldsymbol{L}_o \approx \sum_{j=1}^{k} \boldsymbol{T}^*(t_j)\boldsymbol{C}^*\boldsymbol{C}\boldsymbol{T}(t_j)\delta_j = \tilde{\boldsymbol{L}}_o\tilde{\boldsymbol{L}}_o^*$$

where δ_j are the quadrature weights. The Gramians are thus approximated with low-rank Cholesky factors $\tilde{\boldsymbol{L}}_o \in \mathcal{R}^{n\times kr}$ and $\tilde{\boldsymbol{L}}_c \in \mathcal{R}^{n\times kp}$, respectively, given by

$$\tilde{\boldsymbol{L}}_c = (\boldsymbol{T}(t_1)\boldsymbol{B}\sqrt{\delta_1}, \ldots, \boldsymbol{T}(t_k)\boldsymbol{B}\sqrt{\delta_k})$$

$$\tilde{\boldsymbol{L}}_o = (\boldsymbol{T}^*(t_1)\boldsymbol{C}^*\sqrt{\delta_1}, \ldots, \boldsymbol{T}^*(t_k)\boldsymbol{C}^*\sqrt{\delta_k})$$

For our case, with $p = 3$ and $r = 2$, the columns

$$\boldsymbol{T}(t_i)\boldsymbol{B} = (\boldsymbol{T}(t_i)\boldsymbol{B}_1, 0, \boldsymbol{T}(t_i)\boldsymbol{B}_2)$$

contain snapshots of the state at time t_i, resulting from impulse responses of $\boldsymbol{B}_1$ and $\boldsymbol{B}_2$. In a similar manner,

$$\boldsymbol{T}^*(t_i)\boldsymbol{C}^* = (\boldsymbol{T}^*(t_i)\boldsymbol{C}_1^*, \boldsymbol{T}^*(t_i)\boldsymbol{C}_2^*)$$

contain snapshots of the adjoint state at time t_i resulting from impulse responses of each output. Note that for every additional input (output), the Cholesky factor $\tilde{\boldsymbol{L}}_c$ ($\tilde{\boldsymbol{L}}_o$) increases with k columns.

Similar to the Krylov subspace presented earlier to compute global eigenmodes and optimal disturbances, the Cholesky factors are constructed from simulations of the forward and adjoint systems. The method is therefore matrix-free and based on the employment of a time stepper. The SVD problem (15) can then be approximated as

$$\tilde{\boldsymbol{L}}_o^*\tilde{\boldsymbol{L}}_c = \tilde{\boldsymbol{U}}\,\tilde{\boldsymbol{\Sigma}}\,\tilde{\boldsymbol{V}}^*$$

where $\tilde{\boldsymbol{\Sigma}}$ contains the approximate HSV. The SVD is of the size $kr \times kp$ and is small when the number of snapshots m times the number of inputs p or outputs r is significantly smaller than the number of states n. If either the number of inputs or the number of outputs is large, the output projection method of [20] can be employed. The approximate biorthogonal balanced modes and the reduced-order model are then computed from the expressions (12) and (16). Note that the reduced-order model $\tilde{\boldsymbol{G}}_m$, computed using the low-rank Cholesky factors, is not guaranteed to be stable.

E. Results

1. *Performance of Reduced-Order Model*

Figure 8 shows the spectrum (HSV) and two eigenfunctions (balanced modes) computed by the snapshot method. The first balanced mode and its associated adjoint mode are shown in Figs. 8b and 8c. The singular values come in pairs [4,21,22], and therefore the second and fourth balanced modes look like the first and third modes, respectively, but shifted in the streamwise direction. We observe that the leading balanced mode (Fig. 8b) appears as a wave packet located at the downstream end of the domain, whereas the adjoint balanced mode (Fig. 8c) is an upstream-tilted structure located at the upstream end of the domain. The adjoint modes are similar to the linear optimal disturbances shown in Fig. 4b, and the balanced modes are similar to global eigenmodes shown in Fig. 3b. The adjoint balanced modes thus account for the output sensitivity, and the direct balanced modes account for the most energetic structures.

The projection of the full Navier–Stokes equations on the balanced modes results in the reducer-order model $\boldsymbol{G}_m$ given by Eq. (12). The model reduction error (17) is shown in Fig. 9a, together with the theoretical bounds given by the Hankel singular values. The infinity

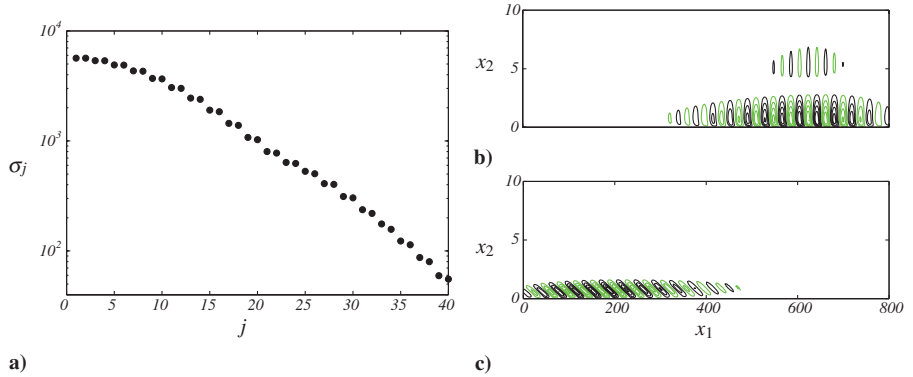

Fig. 8 Plots of a) singular values of Hankel operator, b) streamwise velocity component of the first direct modes, and c) its associated adjoint mode.

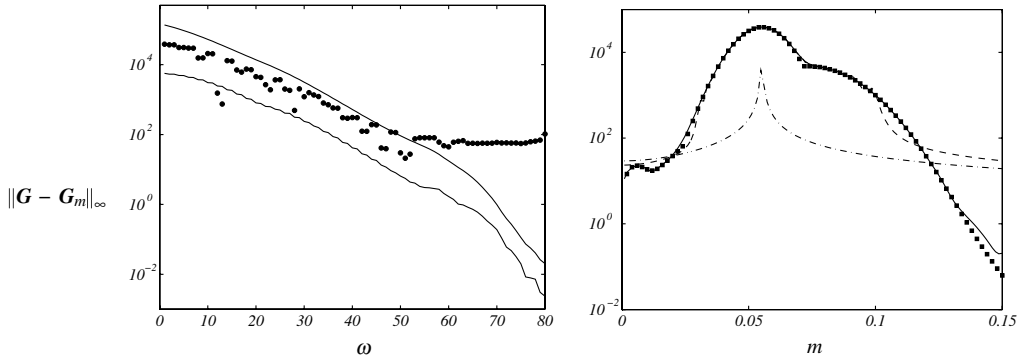

Fig. 9 Plots of a) the error at capturing the peak frequency (black circles) and the upper and lower theoretical bounds (black lines) and b) the largest singular values σ of the transfer function $|G(i\omega)|$ from all input to all outputs computed using the time stepper (squares). The largest response is for $\omega = 0.051$ with a peak value of 4×10^4. The frequency response of the reduced model shown with rank 2 (dashed-dotted lines), 40 (dashed lines), and 70 (solid lines).

norm of the transfer function equals the peak value of the frequency response. Estimating the model reduction error amounts to the calculation of the difference of the peak values of the reduced-order and the Navier–Stokes systems. We observe that the error norm remains approximately within the bounds given by the Hankel singular values for the first 50 modes. Higher modes become increasingly ill-conditioned and, as a consequence, the numerical round-off errors increase, the biorthogonality condition is gradually lost, and the reduced system is no longer balanced. However, the singular values shown in Fig. 8a decrease rapidly, indicating that the I/O behavior of the chosen setup can be captured by a low-dimensional model.

To investigate this further, the amplitudes of the transfer functions with $s = i\omega$ (i.e., the frequency response) are displayed in Fig. 9b for reduced-order models of order $m = 2$, 40, and 70 and for the full DNS model of order 10^5. All frequencies in the interval [0, 0.13] are amplified, and the most dangerous frequency (i.e., the peak response) is approximately $\omega = 0.051$. From Fig. 9b, we observe that the reduced-order model of order 2 captures the most important aspect of the input–output behavior, which is the response of the most dangerous frequency. The model with 40 modes is able to estimate the gains of all the amplified frequencies, but fails to capture the damped low and high frequencies. Adding 30 additional modes results in a model that preserves the input–output behavior correctly for nearly all frequencies.

Finally, the impulse responses from all inputs to all outputs of the reduced-order model (12) are compared with the full Navier–Stokes system (9). In Fig. 10, signals $\boldsymbol{B}_1 \rightarrow \boldsymbol{C}_1$, $\boldsymbol{B}_1 \rightarrow \boldsymbol{C}_2$ and $\boldsymbol{B}_2 \rightarrow \boldsymbol{C}_1$ are shown with black lines. The response of $\boldsymbol{C}_2$ to forcing in $\boldsymbol{B}_2$ is zero, because disturbances traveling upstream are quickly damped. These impulse responses were obtained by using the time stepper with $\sim 10^5$ degrees of freedom. The impulse responses of the reduced-order model (12) with $m = 70$ given by $\boldsymbol{y}(t) = \boldsymbol{C}_m e^{\boldsymbol{A}_m t}\boldsymbol{B}_m$ are shown with red dashed lines. We observe that the reduced-order model registers the same signal as the full model from all inputs to all outputs. The wave packet triggered by the impulse of $\boldsymbol{B}_1$ reaches the first sensor $\boldsymbol{C}_2$ after 500 time units and reaches the second sensor $\boldsymbol{C}_1$ after 1500 time units. The wave packet triggered from the actuator $\boldsymbol{B}_2$ reaches the second sensor after 600 time units.

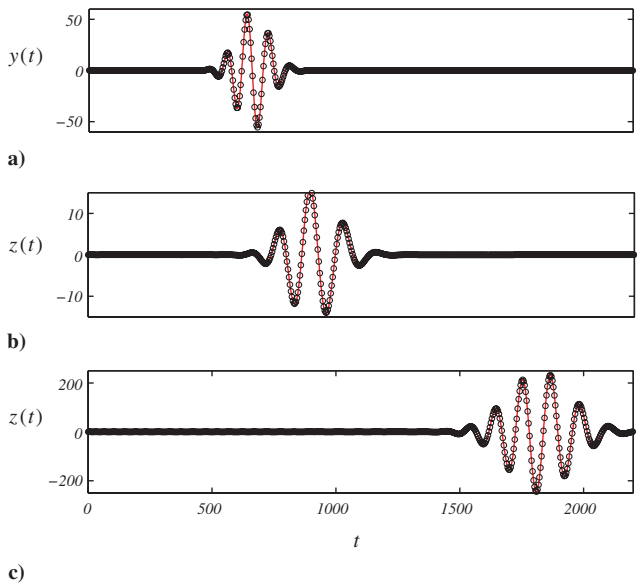

Fig. 10 The impulse response from a) $\boldsymbol{B}_1 \rightarrow \boldsymbol{C}_2$, b) $\boldsymbol{B}_2 \rightarrow \boldsymbol{C}_1$, and c)$\boldsymbol{B}_1 \rightarrow \boldsymbol{C}_1$. The black solid line represents direct numerical simulations with 10^5 degrees of freedom and the red dashed line the balanced reduced-model with 50 degrees of freedom.

2. *Performance of Controller*

In this section, a reduced-order feedback controller is developed with the same dimension as the reduced-order model ($m = 70$) of the previous section. The closed-loop behavior of the system and the objective function will be investigated and compared with the uncontrolled case for the flat-plate boundary-layer flow. In particular, the output z of the closed loop [i.e., the controller (11) $\boldsymbol{G}_c$ connected to the full Navier–Stokes model (5) $\boldsymbol{G}$] is compared with the linearized Navier–Stokes equations without control when the system is forced with stochastic excitation or initiated with an optimal disturbance.

Three controllers are investigated: 1) inexpensive control and low noise contamination with control penalty $l = 1$ and noise parameter $\alpha = 10^2$, 2) expensive control and high noise contamination with $l = 10^2$ and $\alpha = 10^7$, and 3) an intermediate case with $l = 10$ and $\alpha = 10^5$.

The performance of the inexpensive controller in case 1 for the control of the optimal initial condition discussed in Sec. II is examined first. This is interesting, because the controller is not designed specifically for this configuration and it only has a limited window in time to counteract the disturbances that are propagating through the domain in the form of a localized wave packet. In Fig. 11a, the full domain kinetic energy as a function of time is shown as a solid black line for the uncontrolled evolution and as a dashed line for the controlled case. The effect of the controller is evident. The measurement signal detected by the sensor $\boldsymbol{C}_2$ is shown in Fig. 11b, revealing that the sensor picks up the front of the wave packet arriving at $t \approx 350$. A time lag of $\approx$300, consistent with the speed of the propagating wave packet ($0.3U\infty$), is observed until the controller starts acting on the information (see Fig. 11c). The downstream measurement (i.e., the objective function to be minimized) is shown in Fig. 11d as a black solid line for the uncontrolled case and as a dashed black line for the controlled case. It

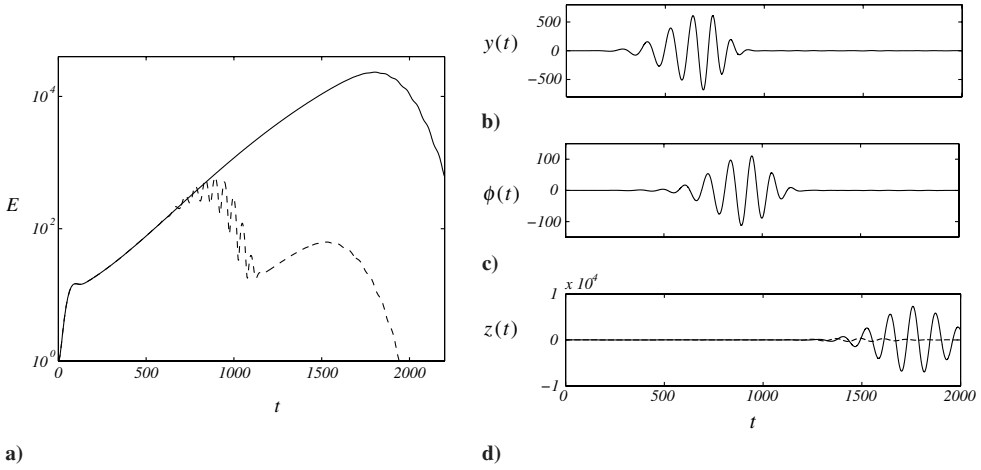

Fig. 11 Control of the wave packet due to the worst-case initial condition: a) uncontrolled energy evolution (as in Fig. 5b) (solid black line) and the energy for the inexpensive controller (dashed black line) , b) output signal as measured by the sensor C_2 driving the controller, c) control signal fed into the wall actuator, and d) signals from the sensor C_1 measuring the objective function. The solid black line shows uncontrolled case, and the dashed black line shows the controlled case.

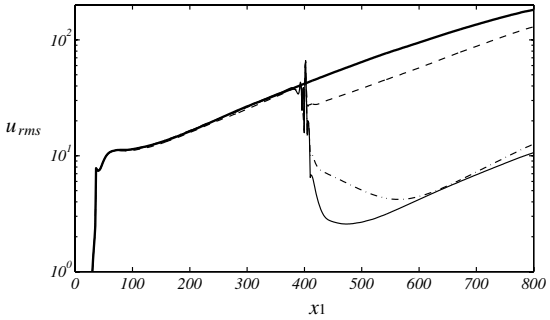

Fig. 12 The rms values of the uncontrolled system (thick solid line), inexpensive controller (solid black line), intermediate controller (dashed-dotted line) and expensive controller (dashed line).

can be seen that also this measure shows a satisfactory performance of the controller.

The three different controllers are tested on a flow case that is forced by the upstream disturbance input $\boldsymbol{B}_1$ with a random time signal. The wall-normal maximums of the rms values of the streamwise velocity component in cases with and without control are shown in Fig. 12. The rms value grows exponentially downstream in the uncontrolled case until the fringe region at $x_1 = 800$. The rms of the controlled perturbation grows only until it reaches the actuator position, where it immediately begins to decay. At the location of the objective function $\boldsymbol{C}_1$ ($x_1 = 750$), the amplitude of the perturbations is 1 order of magnitude smaller than in the uncontrolled case for the less expensive controller. The rms values in the case of the expensive (case 2) and intermediate control (case 3) are shown with dashed and dashed-dotted lines, respectively. The expensive control is very conservative, as the measurement signals are highly corrupted and the control effort is limited: it results only in a small damping of the disturbances. The intermediate controller (case 3) is more cautious in reducing the perturbation energy just downstream of the actuator when compared with the inexpensive controller. Note, however, that at the location in which the objective function is measured, the disturbance amplitude has decreased nearly as much as with the inexpensive controller, although the total perturbation energy is larger over the entire domain.

Table 1 Overview of the eigenvalue problems discussed in this Lecture

Modes	Eigenvalue problem	Method
Global modes	$\boldsymbol{T} = \boldsymbol{U}\boldsymbol{\Sigma}\boldsymbol{U}^{-1}$	Arnoldi
Optimal disturbances	$\boldsymbol{T}^*\boldsymbol{T} = \boldsymbol{U}\boldsymbol{\Sigma}\boldsymbol{U}^*$	Arnoldi
Balanced modes	$\boldsymbol{P}\boldsymbol{Q} = \boldsymbol{U}\boldsymbol{\Sigma}\boldsymbol{U}^{-1}$	Snapshot

IV. Conclusions

Two prerequisites for successful control design are stability analysis and model reduction. The former provides a sound understanding of the instabilities, sensitivities, and growth mechanisms in the flow, and the latter provides a simple and small model that is able to capture the essential dynamics. This preparatory work for control design amounts to solving various large eigenvalue problems, as listed in Table 1. The short-time and asymptotic behavior of disturbances can be completely characterized by the solution of two large eigenvalue problems involving the evolution operator of the linearized Navier–Stokes equations $\boldsymbol{T}$. The global spectrum of $\boldsymbol{T}$ determines the asymptotic growth/decay, dominant temporal frequencies, and the dominant spatial location of instabilities. The global spectrum of $\boldsymbol{T}^*\boldsymbol{T}$ determines the short-time growth/decay of disturbances and the spatial structure of the most dangerous disturbances. This knowledge is indispensable for actuator and sensor placements. Sensors are placed where the flow energy is large, and actuators are placed where the flow sensitivity is large, to minimize the input effort. Because the relation between a few inputs and outputs has much simpler dynamics than the instability, a reduced-order model can be constructed by solving a third eigenvalue problem involving the inputs, outputs, and evolution operator. This results in the balanced modes. The computation of the three sets, global eigenmodes, optimal disturbances, and balanced modes is performed only with a time stepper and without storing large matrices. When the entire flow dynamics are of interest, the high dimensions of the state require iterative techniques. When the I/O behavior is of interest, on the other hand, computational tractability depends on the number of inputs and outputs. Therefore, the snapshot method can be employed in the case of few inputs and outputs. The results of this Lecture also enhance our previous work [4] by incorporating actuation and sensing at the wall. The next step toward applying the controller in experiments is to design a similar control strategy for three-dimensional disturbances in the Blasius flow. Rows of localized actuators and sensors at the wall in the spanwise direction and more realistic disturbance environments such as freestream turbulence will be modeled.

Appendix A: Inputs And Outputs

The expression of inputs $\boldsymbol{B}_1$ and $\mathbf{u}_w$ and outputs $\boldsymbol{C}_1$ and $\boldsymbol{C}_2$ are given in this Appendix. For clarity, we denote the streamwise coordinate with x and the wall-normal component with y. The input

$\boldsymbol{B}_1$ is modeled by a Gaussian type of volume forcing:

$$\begin{bmatrix} \sigma_{w,x}\gamma_{w,y} \\ -\sigma_{w,y}\gamma_{w,x} \end{bmatrix} \exp(-\gamma_{w,x}^2 - \gamma_{w,y}^2) \qquad \gamma_{w,x} = \frac{x - x_w}{\sigma_{w,x}}$$

$$\gamma_{w,y} = \frac{y - y_w}{\sigma_{w,y}}$$

where $\sigma_{w,x} = 4$ and $\sigma_{w,y} = 0.25$ determine the width and height of the function of the function centered around $x_w = 35$ and $y_w = 1$. The actuator in this case is a localized zero-mass-flux actuation on the wall-normal velocity $\mathbf{u}_w = (0, v_w)^T$ at the lower wall given by

$$v_w(x) = \left(1 - \left(\frac{x - x_u}{\sigma_{u,x}}\right)^2\right) \exp\left(-\frac{(x - x_u)^2}{2\sigma_{u,x}^2}\right)$$

with the width $\sigma_{u,x} = 2.5$ and centered at $x_u = 400$. Finally, both measurements extract approximately the wall-normal derivative of the streamwise velocity component (wall shear stress) in limited regions at the wall:

$$\int_\Omega \begin{pmatrix} \gamma_{s,x}\gamma_{s,y}\mathcal{D}_y & 0 \end{pmatrix} \begin{pmatrix} u \\ v \end{pmatrix} \mathrm{d}\Omega \qquad \gamma_{s,x} = \exp\left(-\frac{(x - x_s)^2}{\sigma_{s,x}^2}\right)$$

$$\gamma_{s,y} = \frac{1}{\sigma_{s,y}} \exp\left(-\frac{y^2}{\sigma_{s,y}^2}\right)$$

where $x_e = 300$ for the output $\boldsymbol{C}_2$ and $x_e = 750$ for $\boldsymbol{C}_1$. The width of the regions are determined by $\sigma_{s,x} = 5$ for both sensors. The operator $\mathcal{D}_y$ denotes the y derivative. The y-dependent weighting relies on a width parameter $\sigma_{s,y} = 0.05$. Note that in the limit $\sigma_{s,y} \to 0$, the function approaches the delta function so that Eq. (B1) defines the exact wall shear stress at the wall. The reason for using an approximation to the wall shear stress is the need for an adjoint sensor $\boldsymbol{C}^*$ (see Sec. III.C), which is derived with the respect to the signal to state inner product [4]

$$(r, \boldsymbol{C}\mathbf{u})_s = (\boldsymbol{C}^* r, \mathbf{u})_\Omega$$

These inner products are defined as

$$(r, s)_s = s^T r \qquad (\mathbf{p}, \mathbf{q})_\Omega = \int_\Omega \mathbf{p}^T \mathbf{q} \mathrm{d}\Omega$$

for the scalars s and k and the states $\mathbf{q}$ and $\mathbf{p}$. The adjoint sensor obtained from this definition is, in other words,

$$(r, \boldsymbol{C}\mathbf{u})_s = \int_\Omega r^T \begin{pmatrix} \gamma_{s,x}\gamma_{s,y}\mathcal{D}_y & 0 \end{pmatrix} \mathbf{u} \mathrm{d}\Omega = \int_\Omega r^T \begin{pmatrix} \frac{2y\gamma_{s,x}\gamma_{s,y}}{\sigma_{s,y}^2} & 0 \end{pmatrix} \times \mathbf{u} \mathrm{d}\Omega = (\boldsymbol{C}^* r, \mathbf{u})_{\hat{\Omega}}$$

where we have used integration by parts and the boundary conditions in y. This leads to the recognition of the adjoint sensor in the definition of the observability Gramian (14) as

$$\boldsymbol{C}^* = \begin{pmatrix} 2y\gamma_{s,x}\gamma_{s,y}/\sigma_{s,y}^2 \\ 0 \end{pmatrix}$$

Appendix B: Lifting Procedure

In the same manner as [13], the solution $\mathbf{u}$ is split into a homogeneous part $\mathbf{u}_h$ and a particular part $\mathbf{u}_p$, so that $\mathbf{u} = \mathbf{u}_h + \mathbf{u}_p$. The particular solution fulfills the boundary conditions

$$\dot{\mathbf{u}}_p = \boldsymbol{A}\mathbf{u}_p \qquad \mathbf{u}_p(t) = (0, v_w)^T \varphi(t) \quad \text{at } x_2 = 0 \tag{B1}$$

and the homogeneous part satisfies homogeneous boundary conditions. In principle, we can seek any solution $\mathbf{u}_p$ of the preceding system, but one suitable choice is to use the steady state $\boldsymbol{A}\mathbf{u}_p = 0$. This is obtained by marching the DNS in time subject to steady ($\varphi = 1$) wall blowing v_w until a stationary state $\dot{\mathbf{u}}_p = 0$ is obtained. In the following, we denote this solution as $\boldsymbol{Z}$. The inhomogeneous boundary condition is satisfied by this solution, enabling us to write the particular solution for all times as $\mathbf{u}_p = \boldsymbol{Z}\varphi(t)$, implying that the total field is given by $\mathbf{u} = \mathbf{u}_h + \boldsymbol{Z}\varphi(t)$. Again, expressing the equation for $\mathbf{u}$ in terms of the homogeneous and particular solution, we get

$$\dot{\mathbf{u}}_h = \boldsymbol{A}\mathbf{u}_h + \boldsymbol{A}\boldsymbol{Z}\varphi - \boldsymbol{Z}\dot{\varphi} = \boldsymbol{A}\mathbf{u}_h + \boldsymbol{B}_2\dot{\varphi} \tag{B2}$$

where $\boldsymbol{A}\boldsymbol{Z} = 0$. Further, we have defined the input operator $\boldsymbol{B}_2 = -\boldsymbol{Z}$ for the homogeneous system. The evolution of state and φ can be written as an augmented system for $\hat{\mathbf{u}} = (\mathbf{u}_h, \varphi)^T$ as

$$\dot{\hat{\mathbf{u}}} = \hat{\boldsymbol{A}}\,\hat{\mathbf{u}} + \hat{\boldsymbol{B}}_2\phi$$

where

$$\hat{\boldsymbol{A}} = \begin{pmatrix} \boldsymbol{A} & 0 \\ 0 & 0 \end{pmatrix} \qquad \hat{\boldsymbol{B}}_2 = \begin{pmatrix} \boldsymbol{B}_2 \\ 1 \end{pmatrix} \qquad \phi = \dot{\varphi}$$

Note that in the lifted system (B2) the control signal is given by the time derivative of the boundary control signal, $\phi = \dot{\varphi}$. Similarly, the input operator $\boldsymbol{B}_1$ is extended to $\hat{\boldsymbol{B}}_1 = (\boldsymbol{B}_1, 0)^T$ and the outputs are augmented to $\hat{\boldsymbol{C}}_1 = (\boldsymbol{C}_1, \boldsymbol{C}_1\boldsymbol{Z})$ and $\hat{\boldsymbol{C}}_2 = (\boldsymbol{C}_2, \boldsymbol{C}_2\boldsymbol{Z})$.

Acknowledgments

The authors would like to thank Antonios Monokrousos for assisting in the implementations and Onofrio Semeraro for his comments on the manuscript. The financial support from the Swedish Research Council (VR) is gratefully acknowledged.

References

[1] Barkley, D., Gomes, M. G., and Henderson, R. D., "Three-Dimensional Instability in Flow over a Backward-Facing Step," *Journal of Fluid Mechanics*, Vol. 473, 2002, pp. 167–190. doi:10.1017/S002211200200232X

[2] Blackburn, A. M., Barkley, D., and Sherwin, S., "Convective Instability and Transient Growth in Flow over a Backward-Facing Step," *Journal of Fluid Mechanics*, Vol. 603, 2008, pp. 271–304. doi:10.1017/S0022112008001109

[3] Bagheri, S., Schlatter, P., Schmid, P., and Henningson, D. S., "Global Stability of a Jet in Crossflow," *Journal of Fluid Mechanics* (to be published).

[4] Bagheri, S., Brandt, L., and Henningson, D. S., "Input–Output Analysis, Model Reduction and Control Design of the Flat-Plate Boundary Layer," *Journal of Fluid Mechanics*, Vol. 620, 2009, pp. 263–298. doi:10.1017/S0022112008004394

[5] Schmid, P. J., and Henningson, D. S., *Stability and Transition in Shear Flows*, Springer–Verlag, New York, 2001.

[6] Huerre, P., and Monkewitz, P., "Local and Global Instabilities in Spatially Developing Flows," *Annual Review of Fluid Mechanics*, Vol. 22, 1990, pp. 473–537. doi:10.1146/annurev.fl.22.010190.002353

[7] Chomaz, J. M., "Global Instabilities in Spatially Developing Flows: Nonnormality and Nonlinearity," *Annual Review of Fluid Mechanics*, Vol. 37, 2005, pp. 357–392. doi:10.1146/annurev.fluid.37.061903.175810

[8] Schmid, P. J., "Nonmodal Stability Theory," *Annual Review of Fluid Mechanics*, Vol. 39, 2007, pp. 129–162. doi:10.1146/annurev.fluid.38.050304.092139

[9] Barkley, D., Blackburn, H., and Sherwin, S. J., "Direct Optimal Growth Analysis for Time-Steppers," *International Journal for Numerical Methods in Fluids*, Vol. 57, 2008, pp. 1435–1458. doi:10.1002/fld.1824

[10] Kim, J., and Bewley, T. R., "A Linear Systems Approach to Flow Control," *Annual Review of Fluid Mechanics*, Vol. 39, 2007, pp. 383–417. doi:10.1146/annurev.fluid.39.050905.110153

[11] Bagheri, S., Hoepffner, J., Schmid, P., and Henningson, D., "Input–Output Analysis and Control Design Applied to a Linear Model of Spatially Developing Flows," *Applied Mechanics Reviews*, Vol. 62, No. 2, 2009, Paper 020803. doi:10.1115/1.3077635

[12] Högberg, M., and Henningson, D. S., "Linear Optimal Control Applied

to Instabilities in Spatially Developing Boundary Layers," *Journal of Fluid Mechanics*, Vol. 470, 2002, pp. 151–179. doi:10.1017/S0022112002001702

[13] Högberg, M., Bewley, T. R., and Henningson, D. S., "Linear Feedback Control and Estimation of Transition in Plane Channel Flow," *Journal of Fluid Mechanics*, Vol. 481, 2003, pp. 149–175. doi:10.1017/S0022112003003823

[14] Högberg, M., Bewley, T. R., and Henningson, D. S., "Relaminarization of $Re_{\tau}au = 100$ Turbulence Using Gain Scheduling and Linear State-Feedback Control Flow," *Physics of Fluids*, Vol. 15, 2003, pp. 3572–3575. doi:10.1063/1.1608939

[15] Hoepffner, J., Chevalier, M., Bewley, T. R., and Henningson, D. S., "State Estimation in Wall-Bounded Flow Systems Part 1: Laminar Flows," *Journal of Fluid Mechanics*, Vol. 534, 2005, pp. 263–294. doi:10.1017/S0022112005004210

[16] Chevalier, M., Hoepffner, J., Bewley, T. R., and Henningson, D. S., "State Estimation in Wall-Bounded Flow Systems Part 2: Turbulent Flows," *Journal of Fluid Mechanics*, Vol. 552, 2006, pp. 167–187. doi:10.1017/S0022112005008578

[17] Chevalier, M., Hœpffner, J., Åkervik, E., and Henningson, D. S., "Linear Feedback Control and Estimation Applied to Instabilities in Spatially Developing Boundary Layers," *Journal of Fluid Mechanics*, Vol. 588, 2007, pp. 163–187. doi:10.1017/S0022112007007392

[18] Monokrousos, A., Brandt, L., Schlatter, P., and Henningson, D. S., "DNS and LES of Estimation and Control of Transition in Boundary Layers Subject to Freestream Turbulence," *International Journal of Heat and Fluid Flow*, Vol. 29, No. 3, 2008, pp. 841–855. doi:10.1016/j.ijheatfluidflow.2008.03.009

[19] Moore, B., "Principal Component Analysis in Linear Systems: Controllability, Observability, and Model Reduction," *IEEE Transactions on Automatic Control*, Vol. 26, No. 1, 1981, pp. 17–32. doi:10.1109/TAC.1981.1102568

[20] Rowley, C. W., "Model Reduction for Fluids Using Balanced Proper Orthogonal Decomposition," *International Journal of Bifurcation and Chaos in Applied Sciences and Engineering*, Vol. 15, No. 3, 2005, pp. 997–1013. doi:10.1142/S0218127405012429

[21] Ilak, M., and Rowley, C. W., "Modeling of Transitional Channel Flow Using Balanced Proper Orthogonal Decomposition," *Physics of Fluids*, Vol. 20, 2008, Paper 034103. doi:10.1063/1.2840197

[22] Ahuja, S., Rowley, C. W., Kevrekidis, I. G., and Wei, M., "Low-Dimensional Models for Control of Leading-Edge Vortices: Equilibria and Linearized Models," 45th AIAA Aerospace Sciences Meeting and Exhibit, AIAA Paper 2007-709, 2007.

[23] White, F. M., *Viscous Fluid Flow*, 2nd ed., McGraw–Hill, New York, 1991.

[24] Chevalier, M., Schlatter, P., Lundbladh, A., and Henningson, D. S., "A Pseudo Spectral Solver for Incompressible Boundary Layer Flows," *TRITA-MEK*, Vol. 7, Royal Inst. of Technology, Dept. of Mechanics, Stockholm, 2007.

[25] Nordström, J., Nordin, N., and Henningson, D., "The Fringe Region Technique and the Fourier Method Used in the Direct Numerical Simulation of Spatially Evolving Viscous Flows," *SIAM Journal on Scientific Computing*, Vol. 20, No. 4, 1999, pp. 1365–1393. doi:10.1137/S1064827596310251

[26] Levin, O., and Henningson, D. S., "Exponential vs Algebraic Growth and Transition Prediction in Boundary Layer Flow," *Flow, Turbulence and Combustion*, Vol. 70, No. 1-4, 2003, pp. 183–210. doi:10.1023/B:APPL.0000004918.05683.46

[27] Giles, M. B., and Pierce, N. A., "An Introduction to the Adjoint Approach Design," *Flow, Turbulence and Combustion*, Vol. 65, Nos. 3/4, 2000, pp. 393–415. doi:10.1023/A:1011430410075

[28] Trefethen, L., and Bau, D., *Numerical Linear Algebra*, Society for Industrial and Applied Mathematics, Philadelphia, 1997.

[29] Lehoucq, R., Sorensen, D., and Yang, C., *ARPACK Users' Guide: Solution of Large-Scale Eigenvalue Problems with Implicitly Restarted Arnoldi Methods*, Society for Industrial and Applied Mathematics, Philadelphia, 1998.

[30] Sorensen, D., "Implicit Application of Polynomial Filters in a k Step Arnoldi Method," *SIAM Journal on Matrix Analysis and Applications*, Vol. 13, No. 1, 1992, pp. 357–385. doi:10.1137/0613025

[31] Ehrenstein, U., and Gallaire, F., "On Two-Dimensional Temporal Modes in Spatially Evolving Open Flows: The Flat-Plate Boundary Layer," *Journal of Fluid Mechanics*, Vol. 536, 2005, pp. 209–218. doi:10.1017/S0022112005005112

[32] Akervik, E., Ehrenstein, U., Gallaire, F., and Henningson, D. S., "Global Two-Dimensional Stability Measures of the Flat Plate Boundary Layer Flow," *European Journal of Mechanics, B/Fluids*, Vol. 27, No. 5, 2008, pp. 501–513. doi:10.1016/j.euromechflu.2007.09.004

[33] Cossu, C., and Chomaz, J. M., "Global Measures of Local Convective Instabilities," *Physical Review Letters*, Vol. 78, No. 23, 1997, pp. 4387–4390. doi:10.1103/PhysRevLett.78.4387

[34] Åkervik, E., Hoepffner, J., Ehrenstein, U., and Henningson, D. S., "Optimal Growth, Model Reduction and Control in a Separated Boundary Layer Flow Using Global Eigenmodes," *Journal of Fluid Mechanics*, Vol. 579, 2007, pp. 305–314.

[35] Orr, W. M. F., "The Stability or Instability of the Steady Motions of a Perfect Liquid and of a Viscous Liquid Part 1: A Perfect Liquid," *Proceedings of the Royal Irish Academy, Section A (Mathematical and Physical Sciences)*, Vol. 27, 1907, pp. 9–68.

[36] Orr, W. M. F., "The Stability or Instability of the Steady Motions of a Perfect Liquid and of a Viscous Liquid Part 2: A Viscous Liquid," *Proceedings of the Royal Irish Academy, Section A (Mathematical and Physical Sciences)*, Vol. 27, 1907, pp. 69–138.

[37] Butler, K., and Farrell, B. F., "Three-Dimensional Optimal Perturbations in Viscous Shear Flow," *Physics of Fluids A*, Vol. 4, 1992, pp. 1637–1650. doi:10.1063/1.858386

[38] Curtain, R., and Zwart, H., *An Introduction to Infinite-Dimensional Linear Systems Theory*, Springer–Verlag, New York, 1995.

[39] Zhou, K., Salomon, G., and Wu, E., "Balanced Realization and Model Reduction for Unstable Systems," *International Journal of Robust and Nonlinear Control*, Vol. 9, No. 3, 1999, pp. 183–198. doi:10.1002/(SICI)1099-1239(199903)9:3<183::AID-RNC399>3.0.CO;2-E

[40] Anderson, B., and Moore, J., *Optimal Control: Linear Quadratic Methods*, Prentice–Hall, Upper Saddle River, NJ, 1990.

[41] Zhou, K., Doyle, J., and Glover, K., *Robust and Optimal Control*, Prentice–Hall, Upper Saddle River, NJ, 2002.

[42] Anderson, B., and Liu, Y., "Controller Reduction: Concepts and Approaches," *IEEE Transactions on Automatic Control*, Vol. 34, Aug. 1989, pp. 802–812. doi:10.1109/9.29422

[43] Glover, K., "All Optimal Hankel-Norm Approximations of Linear Multivariable Systems and the L^{∞}-Error Bounds," *International Journal of Control*, Vol. 39, 1999, pp. 1115–1193.

[44] Pernebo, L., and Silverman, L., "Model Reduction via Balanced State Space Representations," *IEEE Transactions on Automatic Control*, Vol. 27, No. 2, 1982, pp. 382–387. doi:10.1109/TAC.1982.1102945

[45] Sirovich, L., "Turbulence and the Dynamics of Coherent Structures I-III," *Quarterly of Applied Mathematics*, Vol. 45, No. 3, 1987, pp. 561–590.

A. Tumin
Associate Editor